

# Advances in the Synthesis and Long-Term Protection of Zero-Valent Iron Nanoparticles

Joshua P. Mehta, Benjamin R. Knappett, Giorgio Divitini, Emilie Ringe, Paul A. Midgley, David Fairen-Jimenez,\* and Andrew E. H. Wheatley\*

Core@shell Fe@Fe<sub>3</sub>O<sub>4</sub> nanoparticles (NPs) are synthesized via the thermal decomposition of iron pentacarbonyl (Fe(CO)<sub>5</sub>) in the presence either of oleylamine (OAm) or a mixture of OAm and oleic acid (OA). The heterostructured nanocomposites formed do so by a postsynthetic modification of isolated Fe seeds. This proves the versatility of the coating procedure and represents a significant advantage over previous work with Co seeds owing to the higher magnetic susceptibility, reduced toxicity, and excellent biocompatibility of Fe. Furthermore, the latter system allows the synthetic methodology to be developed from a two-pot scenario where seeds are isolated then coated, to an easier and more efficient direct one-pot scenario. The two-pot method yields proportionately larger cores. However, in both cases, the monodisperse product reveals a carbonaceous interface between the Fe core and oxide shell. Meanwhile for the one-pot synthesis, the OA:OAm ratio influences both the morphology and dispersity of the product. This is interpreted in terms of competing interactions of the ligands with the iron precursor. Superparamagnetism (SPM) is observed, and microscopic studies reveal oxidative stability of the Fe(0) cores achieved by either method for >6 months. It is proposed that the carbonaceous interface is critical to this sustained oxidative stability.

## 1. Introduction

Magnetic nanoparticles (MNPs) have garnered enormous attention due to their numerous potential applications. These include alternating current (AC) heating for biomedical applications,<sup>[1,2]</sup> magnetic data storage,<sup>[3,4]</sup> magnetic separation,<sup>[5,6]</sup> and catalysis.<sup>[7]</sup> Although a burgeoning area of nanoresearch, substantial barriers remain that have limited advances in the field of magnetic nanomaterials. These generally concern the need for MNPs to exhibit a high degree of monodispersity and a very low level of aggregation.<sup>[2]</sup> Meeting these criteria is essential for the production of reliable and reproducible magnetic responses. MNP size, crystallinity, and magnetic saturation must all be tuned concurrently if applications in, e.g., the biomedical sciences are to be realized.

The study of iron, as the archetypal magnetic material, has gained momentum particularly in a biomedical capacity owing


to its combination of high specific heat loss (SHL), potentially high coercivity, and FDA approval.<sup>[1,8,9]</sup> In this context, Fe is unique amongst other magnetic materials and is consequently a prime candidate in the bioscience field for applications such as targeted drug delivery<sup>[10]</sup> and magnetic resonance imaging.<sup>[11]</sup> Of the many methods of forming iron NPs, the thermal decomposition of Fe(CO)<sub>5</sub> is one of most successful and frequently used techniques.<sup>[12]</sup> The critical diameter,  $D_C$ , for a single magnetic domain in Fe is  $\approx 15$  nm, such that monocrystalline NPs with this mean diameter promise the highest coercivity and magnetic anisotropy.<sup>[13]</sup> However, whereas this is true of Fe(0), the ease with which iron oxidizes<sup>[14]</sup> has meant research has often focused on iron oxide NPs instead.<sup>[15]</sup> This has manifested itself as an extensive interest in superparamagnetic iron oxide nanoparticles (SPIONs).<sup>[16]</sup> However, Fe<sub>3</sub>O<sub>4</sub> has inferior magnetic properties<sup>[17,18]</sup> and, in particular, an SHL only 25% that of the pristine metal, reducing heating effectiveness and having implications for dosage in theranostic applications.<sup>[19]</sup> Crucially, the size limit on magnetically single-domain Fe<sub>3</sub>O<sub>4</sub> is over eight times that of pristine iron.<sup>[13]</sup> This renders the oxide unsuitable for many applications since, for example, particles of such large diameter are unable to cross biological barriers or exhibit lower data storage densities. These drawbacks of iron oxide chemistry have led to research into the protection

J. P. Mehta, Dr. B. R. Knappett, Dr. A. E. H. Wheatley  
Department of Chemistry  
University of Cambridge  
Lensfield Road, Cambridge CB2 1EW, UK  
E-mail: aehw2@cam.ac.uk

Dr. G. Divitini, Dr. E. Ringe, Prof. P. A. Midgley  
Department of Materials Science & Metallurgy  
University of Cambridge  
27 Charles Babbage Road, Cambridge CB3 0FS, UK

Dr. E. Ringe  
Department of Earth Sciences  
University of Cambridge  
Downing Street, Cambridge CB2 3EQ, UK

Dr. D. Fairen-Jimenez  
Department of Chemical Engineering & Biotechnology  
Philippa Fawcett Drive  
Cambridge CB3 0AS, UK  
E-mail: df334@cam.ac.uk

 The ORCID identification number(s) for the author(s) of this article can be found under <https://doi.org/10.1002/ppsc.201800120>.

© 2018 The Authors. Published by WILEY-VCH Verlag GmbH & Co. KGaA, Weinheim. This is an open access article under the terms of the Creative Commons Attribution License, which permits use, distribution and reproduction in any medium, provided the original work is properly cited.

DOI: 10.1002/ppsc.201800120

of nanoparticulate Fe(0) cores based on exploitation of the passive oxidation of Fe. This work has its origins in the recognition that metal oxides often exhibit greater biocompatibility than their parent metals, highlighting the importance of controllably fabricating Fe(0) coated by iron oxide.<sup>[16,20]</sup> Data have suggested that Fe NPs above a diameter of  $\approx 8$  nm retain a stable core coated by an oxide shell following passive oxidation.<sup>[21]</sup> In practice, however, such uncontrolled oxidation leads to smaller and polydisperse cores, meaning larger particles must be formed in the first instance; both a nontrivial task and also one which risks yielding multidomain cores with poor magnetic properties if complete oxidation of individual NPs should occur.<sup>[22]</sup> Generally, oxidation that is not carefully modulated leads to a lowering of the size of the Fe cores in a way that results in sub-optimal magnetic properties.

The inability to furnish satisfactorily protected metal cores by passive oxidation has led to the emergence of a preference for the postsynthetic modification (PSM) of Fe NPs using protective ferrite shells ( $MFe_2O_4$ , where M is typically Mn, Mg, Co, Fe).<sup>[13]</sup> This has avoided reduction in the size of the seed particles. Moreover, being ferrimagnetic, the application of an  $Fe_3O_4$  shell (i.e., M = Fe) enhances the magnetic susceptibility of the particles compared to the use of nonmagnetic coating materials such as silica or precious metals.<sup>[23,24]</sup> Recently the PSM of pristine magnetic seeds by  $Fe_3O_4$  was achieved, with  $Co@Fe_3O_4$  NPs prepared via the sequential thermal decomposition of  $Co_2(CO)_8$  and  $Fe(CO)_5$  in the presence of oleic acid (OA), with the Co(0) cores oxidatively stable for a period of months.<sup>[25]</sup> This was attributed to the formation of a polycrystalline Fe-based shell and the presence of a carbonaceous interface between it and the particle core, preventing epitaxial growth of the latter and providing a barrier to its oxidation. The as synthesized  $Co@Fe_3O_4$  NPs, however, display a dispersity of 9%. This, combined with the documented toxicity<sup>[26]</sup> and inferior magnetic properties<sup>[27]</sup> of Co compared to Fe, renders the system lacking in applicability.

Here we establish the much wider applicability of the methodology used in the PSM of Co(0),<sup>[25]</sup> by applying it successfully to Fe(0). The resulting heterostructures are shown to protect the substantially more oxidatively unstable cores, rendering the final NPs highly magnetic and much more promising candidates for applications requiring low toxicity and biocompatibility.<sup>[16]</sup> We next address problems inherent to the protocol; namely control over dispersity, the production of excess Fe particles during PSM and the effort of isolation and redispersion of the seeds (that will constitute the cores in the final product). In doing so we reveal for the first time a one-pot preparation of  $Fe@Fe_3O_4$  NPs. This direct synthesis suggests the large-scale and highly efficient production of biocompatible NPs with tunable sizes by transferring batch reactor synthesis to the microflow regime where laminar flow conditions can be used to control particle formation.<sup>[28,29]</sup> We succeed also in unequivocally proving the oxidative stability of the as-prepared Fe cores over large time-scales via magnetometric measurements. Furthermore, we probed the origins of this prolonged stability via advanced electron microscopy and spectroscopic techniques and establish the importance of a carbonaceous layer at the metal–oxide interface. We propose that in the present system this interfacial region is essential if adequate protection of zero-valent Fe is to be achieved.

## 2. Results and Discussion

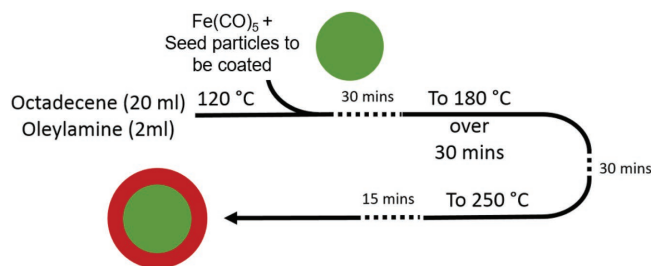
### 2.1. PSM of Fe Seeds

To prove the generality of a recently published procedure for synthesizing  $Co@Fe_3O_4$  NPs,<sup>[25]</sup>  $Co_2(CO)_8$  was replaced by  $Fe(CO)_5$  in octadec-1-ene and oleylamine (OAm) in order to furnish OAm-capped Fe seed particles. Redispersion in hexane<sup>[30]</sup> allowed facile coating using a further dose of  $Fe(CO)_5$  (Scheme 1).

Transmission electron microscope (TEM) analysis of the product revealed heterostructured NPs based on a core@shell architecture in which the shell constituted a 2–3 nm coating. We attribute the lower contrast properties of the shell in bright field (BF) imaging (Figure 1a) to oxidation that occurred when the particles were transiently exposed to air during sample preparation for analysis.<sup>[25]</sup> The step-wise nature of the protocol made characterization of the seeds possible, with these revealing a mean size distribution (MSD) prior to coating of  $7.6 \pm 1.2$  nm, with passive oxidation evident (Figures S1–S3 in the Supporting Information). After PSM with further  $Fe(CO)_5$ , this increased to  $12.3 \pm 1.6$  nm for the core@shell product. However, it is noteworthy that the more strongly contrasting cores now revealed a MSD of  $6.4 \pm 1.3$  nm (Figure S1, Supporting Information). Whilst this MSD agrees (within error) with that of the as-synthesized seeds, the discrepancy before and after coating is better accounted for by the documented expansion in volume that the Fe atomic lattice undergoes upon oxidation (57% expansion in the case of  $Fe_3O_4$ ).<sup>[21]</sup> Thus, the passive formation of an oxide layer at the surface of the uncoated Fe seed particles (Figure S2, Supporting Information) can account for the observed increase in MSD of the as-synthesized Fe NPs relative to that of the cores of the synthetically coated NPs.<sup>[31]</sup>

The distinction between passive (i.e., environmental) oxidation of Fe NP and the synthetic application of an oxide shell becomes obvious if comparing the high-angle annular dark field (HAADF)-scanning TEM (STEM) profiles of the different particle types (Figure 1b,e). Thus, a synthetically coated particle shows a clear drop in signal intensity at the core–shell interface (Figure 1e), indicating a region of lower density. In contrast, the environmental oxidation of Fe NP would be expected to yield a metal–oxide boundary that is either epitaxial, or at which a void gap is present, attributable to the nanoscale Kirkendall effect.<sup>[32]</sup> In the event, such a passively oxidized Fe NP shows a gradual decrease in electron count intensity approaching the particle periphery, suggesting the epitaxial formation of an oxide shell.

Electron energy loss spectra (EELS) line scans confirm the PSM of a pristine Fe core with an oxide shell. Representative



**Scheme 1.** Overview of the sequential preparation of  $Fe@Fe_3O_4$  NPs.

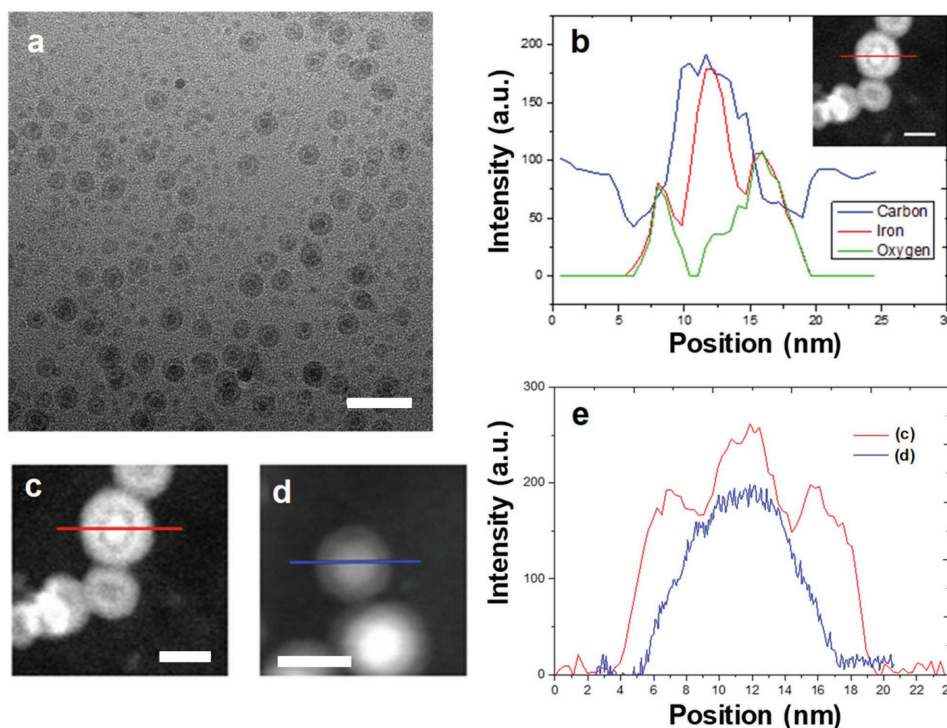


**Figure 1.** a) Representative BFTEM image of freshly coated Fe NPs. b) A representative EELS line scan of a single NP on a  $\text{Si}_3\text{N}_4$  grid revealing distinct carbon minima corresponding to the NP shell and a maximum inside the shell—Inset: line scan position (red). c–e) Representative HAADF-STEM comparison of c) synthetically coated and d) environmentally oxidized Fe NPs with the intensity profiles of the synthetically coated (red) and environmentally oxidized (blue) samples shown in (e) ( $y$ -axis normalised,  $x$ -axis offset to align particle centres), with the respective lines scan positions (correspondingly red and blue) shown in (c) and (d). Scale bars = a) 25 nm and b–d) 10 nm.

Figure 1b and Figure S4 (Supporting Information) show a clear drop in the oxygen signal in the resulting particle cores. In spite of a small amount of carbon contamination, which effect we attribute to the electron beam, it is clear that the drop in oxygen signal corresponds to the occurrence of a carbon maximum at the core–shell interface and which is exactly within the bounds of the two oxygen maxima observed for the shell (Figure 1b). While, to the best of our knowledge, there is no known mechanism that would explain the passive oxidation of an Fe NP to yield carbonaceous material internal to the particle structure, the entrapment of OAm surfactant on the Fe cores as well as incoming OAm from the Fe coating dose explains current observations. Though EELS analysis is conducted on  $\text{Si}_3\text{N}_4$ -supported NPs, the view that OAm may be incorporated into the evolving NPs is consistent with the observation of nitrogen edges in Figure S4 in the Supporting Information. Interestingly, a correspondingly clear nitrogen edge was not observed for the carbonaceous shell in  $\text{Co}@Fe_3O_4$ , the synthesis of which employed OA in place of OAm.<sup>[25]</sup>

The analytical data obtained in the current case strongly suggest that the coating procedure previously used to protect Co seeds, which was shown by a close analysis of the Fe EELS signal to yield  $\text{Co}@Fe_3O_4$  NPs,<sup>[25]</sup> can be adapted to give analogous Fe-core NPs. In fact, the EELS data shown in Figure 1e were acquired 14 d after coating, establishing that PSM results in particle cores that remain unoxidized for weeks. Further, High-resolution (HR) TEM images (Figure S5, Supporting Information) acquired more than 1 year after particle synthesis

indicate that the synthetically coated NPs retain a clear core@shell structure over such timescales.

## 2.2. Direct Formation of $\text{Fe}@Fe_3O_4$ NPs

The extreme oxidative stability imparted to the particle core by nonepitaxial formation of the core@shell structure in the two-step method prompted investigation into reducing the time, effort, and cost associated with PSM by targeting a direct one-step synthesis of stable Fe-based NPs. This would also potentially offer a route by which to transfer particle preparation to the flow regime, promising major advantages over batch processes such as faster reaction times and higher yields.<sup>[33]</sup> Though direct protocols have been reported for the preparation of  $\text{Fe}@Fe_mO_n$  NPs,<sup>[34–36]</sup> these have hitherto produced NPs with suboptimal magnetic properties on account of poor oxidative stability.<sup>[5,37]</sup> Meanwhile, our results (see above, Figure 1d,e) showed clearly that whilst the use of OAm alone without PSM allowed reasonable size control, it resulted in only oxidatively unstable Fe NPs (Figures S2 and S3, Supporting Information). Other attempts to yield crystalline Fe NPs with a high magnetic moment have previously focused on diversifying either the iron precursor (e.g.,  $\text{Fe}[\text{N}(\text{SiMe}_3)_2]_2$ ,<sup>[35]</sup>  $\text{Fe}(\text{C}_5\text{H}_5)(\text{C}_6\text{H}_7)$ <sup>[38])</sup> or the surfactants (e.g., OA,<sup>[22,36]</sup> hexadecylammonium chloride,<sup>[35,39]</sup> hexadecylamine,<sup>[40]</sup> and didodecyltrimethylammonium bromide<sup>[40]</sup>). The use of OA, in particular, was interesting by virtue of the claim that it can produce stable core@shell NPs via

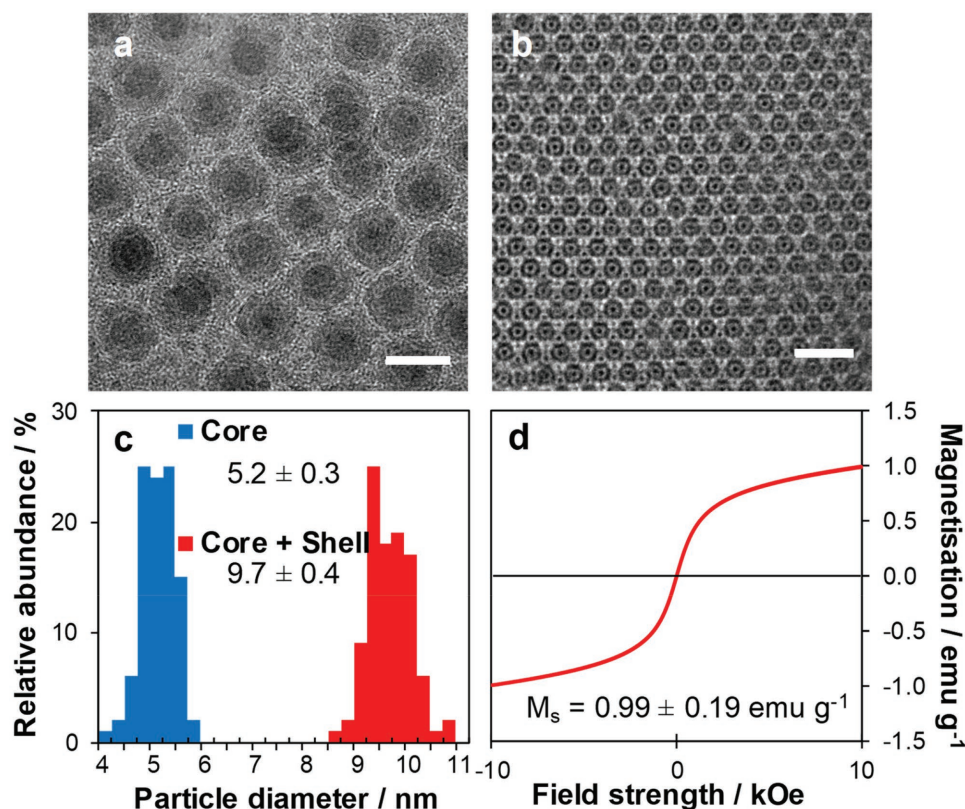


**Figure 2.** Representative BFTEM images of sample **D** (scale bars a) 10 nm, b) 25 nm), alongside c) mean size distributions (in each case,  $N = 100$ ). d) Superparamagnetic response of **D** measured using VSM in the range  $-10$  to  $10$  kOe with field increments of  $100$  Oe.

passive oxidation of Fe seeds.<sup>[12,40]</sup> It has been postulated that the decomposition of an intermediate  $\text{Fe}^{2+}$ -oleate complex, formed when  $\text{Fe}(\text{CO})_5$  is combined with OA,<sup>[41,42]</sup> yields NP seeds that grow at elevated temperature.<sup>[43]</sup> However, in our hands repeated attempts to produce monodisperse particles with long-term oxidative stability using only OA led to particle agglomeration and polydispersity. However, taking these observations together with our data establishing that OAm facilitates  $\text{Fe}(0)$  NP stability, we introduced OAm to the  $\text{Fe}(\text{CO})_5$ -OA reaction mixture.

The OAm:OA ratio in mixed surfactant reactions was varied as shown in Table S1 in the Supporting Information for samples **A-I**. In each case, a 5.7-fold excess of  $\text{Fe}(\text{CO})_5$  was used with respect to total surfactant (OAm + OA; 5.7 being the metal:surfactant ratio employed in the sequential synthesis method, see the Experimental Section). Data revealed that an absence of OA inhibited core@shell NP formation, insinuating a role for OA in defining particle structure (see above and ref. [41]), whilst a low mol% of OAm led to polydispersity and agglomeration (Figure S6, Supporting Information). Of the surfactant mixtures tested, that in sample **D** (28:72 OAm:OA) gave the most monodisperse NPs (Figure 2a,b) and was therefore selected for further investigation.

With the OAm:OA ratio optimized at 28:72, other reaction parameters were modulated (Table 1). Variation of the Fe:surfactant ratio from that in sample **D** (Table S1, Supporting Information) led to increased polydispersity, uncoated Fe seeds, and agglomeration (Figure S7, Supporting Information). In the

case of sample **O**, extended reaction time was needed to ensure complete thermal decomposition of the substrate, suggesting that an increase in surfactant level gives relatively stable iron-surfactant intermediate complexes. Consistent with this is the prior report that decomposition temperature increases with decreasing Fe:surfactant ratio.<sup>[40]</sup> This point is also exemplified by sample **N**, which employed the same Fe:surfactant ratio as sample **D**, but showed no decomposition of  $\text{Fe}(\text{CO})_5$  even after 90 min, as evidenced by the retention of an orange colored reaction mixture. This is consistent with the previous report of no substrate decomposition below  $180$  °C in the presence of OA.<sup>[40]</sup> Further work employing Fe:surfactant and OA:OAm ratios of

**Table 1.** Variation of reaction parameters employing a 28:72 OAm:OA surfactant mixture.

Sample	Temperature [°C]	Fe:surfactant molar ratio	Particle size distribution [nm] <sup>a)</sup>
J	180	10:1	$7.8 \pm 1.3$
K	180	8:1	$8.1 \pm 0.6$
L	240	5.7:1	$5.6 \pm 1.7$
M	200	5.7:1	$6.8 \pm 0.6$
D	180	5.7:1	$9.7 \pm 0.4$
N	160	5.7:1	N/A
O	180	4:1	$8.1 \pm 0.8$

<sup>a)</sup>  $N = 100$ .

5.7:1 and 72:28, respectively, focused on the effect of elevated temperature. TEM analysis of the NPs synthesized at temperatures higher than that used for sample **D** revealed a decrease in particle size (samples **M** and **L**, Table 1; Figures S6 and S7, Supporting Information), attributable to faster substrate decomposition and particle nucleation restricting the growth phase.<sup>[40]</sup> This effect is shown particularly by sample **L**, where Figure S7 in the Supporting Information reveals small particles and limited core@shell NP formation, suggesting a lack of feedstock to either grow the Fe seeds or constitute the shell.

Based on these data, sample **D** remained the most monodisperse sample and was therefore subjected to detailed analysis. BF imaging revealed particles with core@shell structure (Figure 2), with the less strongly contrasting shell suggesting oxidation. Whilst the mean total particle size was  $9.7 \pm 0.4$  nm, that of the core was  $5.2 \pm 0.3$  nm (Figure 2c), rendering both the seeds and core@shell NPs monodisperse ( $\sigma \leq 5\%$ ).<sup>[4]</sup> One consequence of this high level of monodispersity was the observation of regions of superlattice formation (Figure 2b). Stacking gave NP mono-, bi-, and tri- layers, the last in a hexagonal close packed, ABC-type arrangement.<sup>[4]</sup> Lastly, vibrating-sample magnetometry (VSM) measurements indicated a magnetic saturation of  $0.99 \pm 0.19$  emu g<sup>-1</sup> and an absence of hysteresis (Figure 2d). These data are consistent with the superparamagnetic behaviour expected from sub-10 nm nanoparticulate iron.

Moving to HAADF-STEM, data clearly indicate that NPs in sample **D** (prepared by the direct synthesis) exhibit a more complex core@double-shell structure than that suggested by BFTEM imaging (Figure 3a,b). This structure closely resembles that seen for NPs prepared by the two-step method. Syntheses in which an oxidizing agent has been used to form a Fe<sub>3</sub>O<sub>4</sub> shell around a preformed Fe core have hitherto induced the formation of a void space between core and shell.<sup>[44]</sup> This has been attributed to the nanoscale Kirkendall effect.<sup>[45]</sup> In contrast, the present systems demonstrate no hollow particles after months of exposure to an aerobic atmosphere (Figures S5 and S8, Supporting Information). Instead, HRSTEM reveals a lower contrast region between core and outer shell for all particles. In addition to this, triplicated VSM measurements conducted on sample **D** after storage for more than 15 months as a solid under air showed no significant reduction in the magnetic saturation value of the sample over that time ( $0.99 \pm 0.07$  emu g<sup>-1</sup> ( $\approx 0.99 \pm 0.19$  emu g<sup>-1</sup> fresh); Figure S9, Supporting Information). It is noteworthy that samples submitted for HRTEM were all exposed to oxygen-rich plasma for 30 s to oxidatively remove any organic contamination from their exteriors before being introduced to the microscope.<sup>[46,47]</sup> Moreover, for samples that were retained for microscopic reanalysis, the prepared TEM grid was stored under a normal atmosphere for the intervening period, meaning that the NPs withstood prolonged air exposure as a solid thin film rather than being in the relatively protected environment of an anhydrous dispersion. Taken together, these observations establish that the particle cores exhibit significant long-term resistance to oxidation and that this originates from each NP incorporating an interfacial layer of trapped carbonaceous material. This view is supported by electron tomography on sample **D** (Figure S10, Supporting Information), which revealed cores suspended within, but never in direct contact with, their surrounding shells. The failure to observe

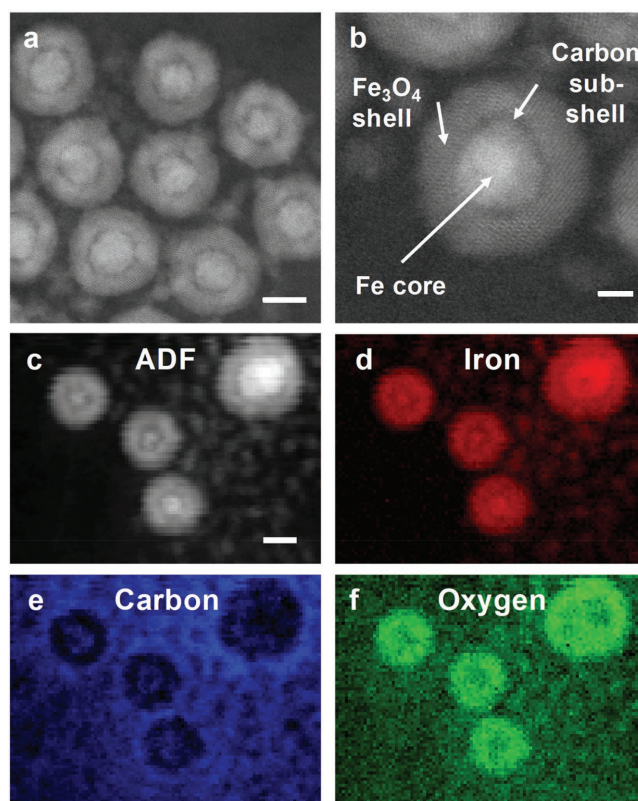


**Figure 3.** a,b) Representative HAADF-STEM images of sample **D** revealing a reproducible core@double-shell architecture after 30 s exposure to an oxygen–argon (25:75) plasma. c) Annular dark field and d–f) EELS spectral imaging of sample **D** showing the presence of iron (red), carbon (blue), and oxygen (green). Scale bars = a,c) 5 nm and b) 2 nm.

a “yolk–shell” type system<sup>[48]</sup> suggests the interstitial layer contains a low density material. EELS mapping adds weight to this thesis by establishing the presence of carbon between the core and outer-shell in addition to a carbon signal derived from surfactant directly bound to the outer surfaces of individual NPs (Figure 3c–f).

HRTEM analysis corroborates the polycrystallinity suggested by HAADF-STEM for the outer shell of NPs prepared using the direct (i.e., one-step) method (Figure 3). Data suggest amorphous particle cores and polycrystalline outer-shells (Figure 2a; Figures S11 and S12, Supporting Information). Interrogation of the lattice fringes in the shells of 20 representative NPs reveals an average *d*-spacing of  $2.54 \pm 0.03$  and  $2.97 \pm 0.07$  Å. These can be attributed to the <311> and <220> planes, respectively, of the two inverse spinel structures of iron oxide, Fe<sub>3</sub>O<sub>4</sub> and its Fe(II)-deficient analogue,<sup>[43]</sup>  $\gamma$ -Fe<sub>2</sub>O<sub>3</sub> (Table S2, Supporting Information).<sup>[49]</sup> This lattice fringe analysis argues against the presence of  $\alpha$ -Fe<sub>2</sub>O<sub>3</sub>.<sup>[50]</sup> However, whilst it is established that Fe<sub>3</sub>O<sub>4</sub> is the preferentially formed oxide under mild (atmospheric) oxidizing conditions,<sup>[51]</sup> such as those used in this work, HRTEM cannot distinguish between Fe<sub>3</sub>O<sub>4</sub> and  $\gamma$ -Fe<sub>2</sub>O<sub>3</sub>.<sup>[25]</sup> STEM-EELS data were therefore acquired and analyzed using multivariate analysis routines. Oxygen edge isolation of acquired EELS maps evidenced a lack of oxygen in the core, corroborating the oxidative stability of the coated seeds (Figure 4a). The core-loss EELS profile

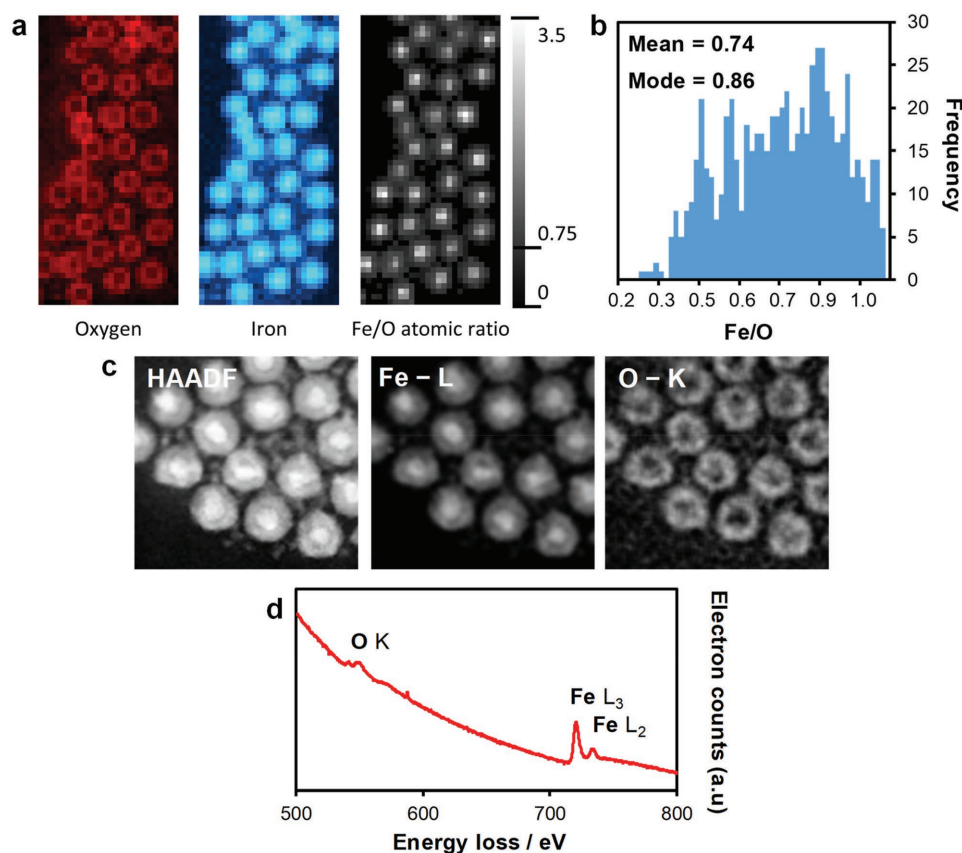


**Figure 4.** a) Iron (blue) and oxygen (red) EELS maps of sample **D**, and b) the Fe:O ratio histogram over 30 NPs. c) STEM-EELS mapping of sample **D**, with Fe-L and O-K edge isolation showing the lack of oxygen in the cores. d) Representative EELS profile of a particle shell constructed from a 5-component image model decomposition.

of the oxide shell (Figure 4), is compatible with both  $\text{Fe}_3\text{O}_4$  and  $\gamma\text{-Fe}_2\text{O}_3$ , which have very similar edges.<sup>[52]</sup> Quantification was therefore sought by comparison of the Fe:O ratio in the shell (0.75 for  $\text{Fe}_3\text{O}_4$ , 0.67 for  $\gamma\text{-Fe}_2\text{O}_3$ ). A histogram was derived from a spectrum image acquired over 30 particles in order to increase the signal-to-noise ratio. This produced modal and mean Fe:O ratios of 0.86 and 0.74 respectively, suggesting  $\text{Fe}_3\text{O}_4$  (Figure 4b). This spread in the observed Fe:O ratio is attributed to spectral averaging, as some pixels contain the core of the particles (and hence have a higher Fe content) and some pixels might also be influenced by the background  $\text{Si}_3\text{N}_4$  support.

As for the two-step synthesis, the formation of NPs that incorporate a trapped carbonaceous layer can be attributed to interaction (and subsequent incorporation within the product) of the surfactant with  $\text{Fe}(\text{CO})_5$ . The reactivity of metal complexes in the presence of surfactant in a nonpolar solvent, such as octadec-1-ene, is influenced by the bond strength between the ligand and the metal precursor.<sup>[53]</sup> In this capacity, amine headgroups (viz. OAm) possess a weaker binding energy to the surface of growing nuclei than do carboxylates (viz. OA).<sup>[40]</sup> Correspondingly, molecular modeling<sup>[54]</sup> has found OA, with its three binding modes (monodentrate, bridging, or chelating), to have a higher probability of coordinating to a crystal surface than does OAm, with its single binding mode. Taken together with the incorporation of a carbonaceous layer within NPs prepared by a two-step method, the current data suggest that in our

direct synthesis, amorphous Fe seeds (Figure S12, Supporting Information) form via the rapid decomposition of OAm-coordinated  $\text{Fe}(\text{CO})_5$  to give OAm-Fe NPs. The polycrystalline shell can be viewed as forming from crystalline OA-Fe NPs that nucleate following the slower solution decomposition of less reactive OA-complexed  $\text{Fe}(\text{CO})_5$  and which then flocculate to the already formed OAm-Fe seed, trapping capping agent at the resulting interface in doing so. To probe this idea, aliquots of the reaction mixture were removed in the course of the direct particle synthesis at time ( $t$ ) = 1, 5, 15, 30, 45, 60, 75, and 90 min after  $\text{Fe}(\text{CO})_5$  injection (Figure S13, Supporting Information). Primary seed particle formation, attributed to the decomposition of OAm-coordinated  $\text{Fe}(\text{CO})_5$ , was observed at  $t = 1$  min., with these primary particles being sustained, without change, for the first three aliquots. At  $t = 30$  min., the first of the larger agglomerates, attributed to flocculation of more slowly nucleated OA-Fe to the OAm-Fe seeds, were observed. Heterostructured NPs were observed at 45 min, with further flocculation of OA-Fe leading to particle growth and the formation of the final core@double-shell structured NPs inside which capping agent is trapped. Lastly, the observation (Figure 3; Figure S14, Supporting Information) of small, crystalline particles outside these core@double-shell NPs, and the confirmed need for an excess of OA to ensure particle heterostructure, is consistent with the solution-nucleation of OA-Fe NPs resulting from the decomposition of OA-coordinated precursor.

### 3. Conclusions

The preparation by a two-step method of oxidatively stable Fe@Fe<sub>3</sub>O<sub>4</sub> nanoparticles has established the versatility of a PSM coating procedure previously limited to protecting toxic NPs. Hence, the effectiveness of the procedure in substantially stabilizing core material with reduced toxicity and greater magnetic permeability has been evidenced. These points are highly relevant for biological applications. Moreover, the NP cores have been shown to be composed of unoxidized iron after 12 months of air exposure. The detection of carbon within the particle structure has reinforced the previously proposed view that these heterostructured particles form by multiple Fe nuclei aggregating at the surfaces of injected seed particles that are capped by surfactant molecules, trapping these organics within the evolving particle structure. Moreover, the incorporation of organic material appears to be responsible for there being a lack of epitaxy between the core and shell of the resulting particles that obviates restrictions to the generality of coating due to lattice mismatch between core and shell.

By exploring the use of a dual surfactant reaction medium (OAm:OA 28:72), core@double-shell particles were prepared in which neither PSM coating nor high temperatures ( $\approx 180$  °C in the direct synthesis vs 250 °C in the two-step protocol) were required. Nevertheless, Fe@Fe<sub>3</sub>O<sub>4</sub> NPs still formed efficiently, with the nature of the oxide confirmed using multivariate analysis of EELS data. The Fe core stability of the directly prepared particles can still be attributed to a carbonaceous interface between the core and Fe<sub>3</sub>O<sub>4</sub> shell, as justified using HAADF-HRSTEM, EELS, and tomography. The presence of this layer is rationalized in terms of the competitive interaction of OAm and OA with iron precursor. The ability to fabricate heterostructured NPs directly suggests the possibility of translating NP synthesis to the flow regime and experiments are now underway to investigate the use of laminar flow conditions in the size regulation of stable heterostructures.

### 4. Experimental Section

*General Synthetic Comments:* Fe(CO)<sub>5</sub> (99.99%), OA (90%), and octadec-1-ene (90%) were purchased from Sigma-Aldrich. OAm (97%) was purchased from Arcos Organics. Anhydrous isopropylalcohol (IPA, 99.5+ %) and ethanol (96%) were purchased from Alfa Aesar and VWR chemicals, respectively. Fresh ethanol was tapped from a still when required, using 3 Å molecular sieves as a desiccant. All chemicals were used as received except for liquids, which were degassed with a stream of dry, oxygen-free N<sub>2</sub> for 2 h immediately before use.

*Sequential Fe@Fe<sub>3</sub>O<sub>4</sub> NP Synthesis—Synthesis of Fe Seeds:* Fe seed NPs were prepared and coated following a modified literature route.<sup>[25]</sup> Typically, Fe(CO)<sub>5</sub> (0.7 mL, 5.2 mmol) was injected into a degassed solution of OAm (0.3 mL, 0.9 mmol) in octadec-1-ene (20 mL) at 180 °C under N<sub>2</sub>. After 30 min., the mixture was allowed to cool to room temperature. The resulting solution was washed with degassed EtOH/IPA (1:1, 40 mL) and redispersed in hexane (3 mL).

*Sequential Fe@Fe<sub>3</sub>O<sub>4</sub> NP Synthesis—Coating Procedure:* Fe(CO)<sub>5</sub> (0.14 mL, 1.0 mmol) was injected into a degassed, vigorously stirred mixture of octadec-1-ene (20 mL) and OAm (2 mL) at 120 °C, followed immediately by seed particles in hexane (3 mL). Gaseous hexane was vented through a septum via a needle under a positive pressure of N<sub>2</sub>. The temperature was maintained at 120 °C for 30 min, after which the needle was removed. The temperature was increased to 180 °C over

30 min ( $\approx 2$  °C min<sup>-1</sup>), held at 180 °C for 30 min, then rapidly increased to 250 °C for 15 min, before being allowed to cool to room temperature. The reaction solution was transferred to a degassed Schlenk tube and the particles sedimented overnight by adding degassed IPA (60 mL). The particles were redispersed in hexane and washed with EtOH, before being centrifuged and redispersed in hexane.

*Direct Fe@Fe<sub>3</sub>O<sub>4</sub> Synthesis:* Representatively, for sample D, Fe(CO)<sub>5</sub> (0.7 mL, 5.2 mmol) was injected into a degassed solution of OAm (0.084 mL, 0.255 mmol) and OA (0.207 mL, 0.657 mmol) in octadec-1-ene (20 mL) at 180 °C under N<sub>2</sub>. After 90 min, the mixture was allowed to cool to room temperature before being injected into degassed acetone and left to sediment. The supernatant was discarded, the NPs dispersed in hexane (3 mL) and the cleaning procedure repeated before the particles were finally sedimented twice through degassed IPA/EtOH (2:1, 60 mL). The NPs were finally redispersed in hexane (3 mL).

*Particle Characterization:* Hexane-dispersed samples were drop-coated onto lacey carbon-coated Cu grids (Agar Scientific, 400 mesh) and Si<sub>3</sub>N<sub>4</sub> membranes (Agar Scientific, 30 nm membrane) before being plasma cleaned (Fischione 1020) to remove surface carbon contamination. A Philips CM200 with a 200 kV field emission gun (FEG) TEM with a Supertwin objective lens was used to obtain the HRTEM images in Figure S5 in the Supporting Information. A FEI Tecnai F20 G2 200 kV FEGTEM with a Gatan image filter (GIF) 200 followed by a 1k x 1k CCD, and a Fischione model 3000 HAADF detector was used to acquire Figures 1a and 2a,b and Figures S2c,d, S6–S8, S11, S13 (Supporting Information). HRSTEM HAADF images and EELS were acquired on an FEI Titan<sup>3</sup> 80–300 mono/C<sub>s</sub> corrected FEGTEM (Figures 1b–e, 3a,b, 4; Figures S2a,b, S3, S4, and S14, Supporting Information) operated at an accelerating voltage of 300 kV. HAADF-STEM tomography set was collected on an FEI Talos F200X using a  $-70^\circ$  to  $+70^\circ$  tilt range and a probe current of 20 pA, with reconstruction performed using Avizo software (Figure S10, Supporting Information). HAADF-EELS data were collected on a CFEG JEOL-F200 at 200 kV (Figure 3c,d). A Princeton Measurements Corporation MicroMag Model 3900 VSM was used to measure the direct magnetic moment versus field strength of samples in a gelatin capsule in the range  $\pm 10$  kOe, with field increments of 100 Oe. Powder X-ray diffraction (PXRD) patterns were measured on a PANalytical Empyrean diffractometer fitted with an X'celerator detector and using a Cu-K $\alpha_1$  ( $\lambda = 1.5406$  Å) source, a step size of 0.002° and a scanning speed of 0.022° s<sup>-1</sup> at 40 kV and 40 mA.

### Supporting Information

Supporting Information is available from the Wiley Online Library or from the author.

### Acknowledgements

The authors wish to thank L. Gontard and A. Fernández for help with the acquisition of data presented in Figures S2 and S3 in the Supporting Information. HAADF-STEM tomography data were collected by A. Carlsson of FEI (Figure S10, Supporting Information). EELS images were collected by A. Yasuhara of JEOL (Figure 3c–f). Thanks go also to S. Datta for assistance with introductory experiments. J.P.M. acknowledges CRUK and the Cambridge Cancer Centre for financial support. D.F.-J. thanks the Royal Society for a University Research Fellowship and the European Research Council (ERC) under the European Union's Horizon 2020 research and innovation programme (NanoMOFdeli), ERC-2016-COG 726380. G.D. and P.A.M. acknowledge funding from ERC grant agreements 291522–3DIMAGE and 312483-ESTEEM2. Open Data for this paper are available at <https://dx.doi.org/10.17863/CAM.23376>.

### Conflict of Interest

The authors declare no conflict of interest.

## Keywords

core@shell, iron, magnetic, nanoparticle, oxidative stability

Received: March 19, 2018

Revised: April 18, 2018

Published online:

- [1] C. S. S. R. Kumar, F. Mohammad, *Adv. Drug Delivery Rev.* **2011**, 63, 789.
- [2] S. Dutz, R. Hergt, *Nanotechnology* **2014**, 25, 452001.
- [3] G. Reiss, A. Hütten, *Nat. Mater.* **2005**, 4, 725.
- [4] S. Sun, C. B. Murray, D. Weller, L. Folks, A. Moser, *Science* **2000**, 287, 1989.
- [5] I. S. Lee, N. Lee, J. Park, B. H. Kim, Y. Yi, T. Kim, T. K. Kim, I. H. Lee, S. R. Paik, T. Hyeon, *J. Am. Chem. Soc.* **2006**, 128, 10658.
- [6] H.-Y. Park, M. J. Schadt, L. Wang, I.-I. S. Lim, P. N. Njoki, S. H. Kim, M.-Y. Jang, J. Luo, C.-J. Zhong, *Langmuir* **2007**, 23, 9050.
- [7] N. Toshima, *Pure Appl. Chem.* **2000**, 72, 317.
- [8] M. Creixell, A. C. Bohórquez, M. Torres-Lugo, C. Rinaldi, *ACS Nano* **2011**, 5, 7124.
- [9] D. Bobo, K. J. Robinson, J. Islam, K. J. Thurecht, S. R. Corrie, *Pharm. Res.* **2016**, 33, 2373.
- [10] N. R. Datta, S. Krishnan, D. E. Speiser, E. Neufeld, N. Kuster, S. Bodis, H. Hofmann, *Cancer Treat. Rev.* **2016**, 50, 217.
- [11] D. Ni, W. Bu, E. B. Ehlerding, W. Cai, J. Shi, *Chem. Soc. Rev.* **2017**, 46, 7438.
- [12] R. Hufschmid, H. Arami, R. M. Ferguson, M. Gonzales, E. Teeman, L. N. Brush, N. D. Browning, K. M. Krishnan, *Nanoscale* **2015**, 7, 11142.
- [13] A. H. Lu, E. L. Salabas, F. Schüth, *Angew. Chem., Int. Ed.* **2007**, 46, 1222.
- [14] N. Tran, T. J. Webster, *J. Mater. Chem.* **2010**, 20, 8760.
- [15] A. P. Reena Mary, T. N. Narayanan, V. Sunny, D. Sakthikumar, Y. Yoshida, P. A. Joy, M. R. Anantharaman, *Nanoscale Res. Lett.* **2010**, 5, 1706.
- [16] M. Angelakeris, *Biochim. Biophys. Acta* **2017**, 1861, 1642.
- [17] R. Hergt, R. Hiergeist, I. Hilger, W. A. Kaiser, Y. Lapatnikov, S. Margel, U. Richter, *J. Magn. Magn. Mater.* **2004**, 270, 345.
- [18] B. Mehdaoui, A. Meffre, J. Carrey, S. Lachaize, L. M. Lacroix, M. Gougeon, B. Chaudret, M. Respaud, *Adv. Funct. Mater.* **2011**, 21, 4573.
- [19] R. Hergt, S. Dutz, *J. Magn. Magn. Mater.* **2007**, 311, 187.
- [20] X. Li, J. Wei, K. E. Aifantis, Y. Fan, Q. Feng, F.-Z. Cui, F. Watari, *J. Biomed. Mater. Res., Part A* **2016**, 104, 1285.
- [21] C. M. Wang, D. R. Baer, L. E. Thomas, J. E. Armonette, J. Antony, Y. Qiang, G. Duscher, *J. Appl. Phys.* **2005**, 98, 094308.
- [22] T. J. Yoon, H. Lee, H. Shao, R. Weissleder, *Angew. Chem., Int. Ed.* **2011**, 50, 4663.
- [23] G. Wang, A. Harrison, *J. Colloid Interface Sci.* **1999**, 217, 203.
- [24] F. Mazaleyrat, M. Ammar, M. LoBue, J. P. Bonnet, P. Audebert, G. Y. Wang, Y. Champion, M. Hÿtch, E. Snoeck, *J. Alloys Compd.* **2009**, 483, 473.
- [25] B. R. Knappett, P. Abdulkin, E. Ringe, D. Jefferson, S. Lozano-Perez, T. C. Rojas, A. Fernández, A. E. H. Wheatley, *Nanoscale* **2013**, 5, 5765.
- [26] L. Leyssens, B. Vinck, C. Van Der Straeten, F. Wuyts, L. Maes, *Toxicology* **2017**, 387, 43.
- [27] C. R. Hammond, D. R. Lide, in *CRC Handbook of Chemistry and Physics* (Ed: J. R. Rumble), 98th ed., CRC Press/Taylor & Francis, Boca Raton, FL **2018**, Chapter 4.
- [28] A. J. Capel, S. Edmondson, S. D. R. Christie, R. D. Goodridge, R. J. Bibb, M. Thurstans, *Lab Chip* **2013**, 13, 4583.
- [29] Z. Gao, T. Ma, E. Zhao, D. Docter, W. Yang, R. H. Stauber, M. Gao, *Small* **2016**, 12, 556.
- [30] C. Wang, S. Peng, L. Lacroix, S. Sun, *Nano Res.* **2009**, 2, 380.
- [31] P. Patnaik, *Handbook of Inorganic Chemicals*, McGraw-Hill Professional, London, UK **2002**.
- [32] Y. Yin, R. M. Rioux, C. K. Erdonmez, S. Hughes, G. Somorjai, A. P. Alivisatos, *Science* **2004**, 304, 711.
- [33] I. R. Baxendale, J. Deeley, C. M. Griffiths-Jones, S. V. Ley, S. Saaby, G. K. Tranmer, *Chem. Commun.* **2006**, 0, 2566.
- [34] D. Farrell, S. A. Majetich, J. P. Wilcoxon, *J. Phys. Chem. B* **2003**, 107, 11022.
- [35] F. Dumestre, B. Chaudret, C. Amiens, P. Renaud, P. Fejes, *Science* **2004**, 303, 821.
- [36] F. Xu, C. Cheng, D. Chen, H. Gu, *ChemPhysChem* **2012**, 13, 336.
- [37] J. Cheng, X. Ni, H. Zheng, B. Li, X. Zhang, *Mater. Res. Bull.* **2006**, 41, 1424.
- [38] S. Cheong, P. Ferguson, K. W. Feindel, I. F. Hermans, P. T. Callaghan, C. Meyer, A. Slocombe, C.-H. Su, F.-Y. Cheng, C.-S. Yeh, B. Ingham, M. F. Toney, R. D. Tilley, *Angew. Chem., Int. Ed.* **2011**, 50, 4206.
- [39] L.-M. Lacroix, N. Frey Huls, D. Ho, X. Sun, K. Cheng, S. Sun, *Nano Lett.* **2011**, 11, 1641.
- [40] G. Singh, P. A. Kumar, C. Lundgren, A. T. J. Van Helvoort, R. Mathieu, E. Wahlström, W. R. Glomm, *Part. Part. Syst. Charact.* **2014**, 31, 1054.
- [41] J. van Wonderghem, S. Morup, S. W. Charles, S. Wells, J. Villadsen, *Phys. Rev. Lett.* **1985**, 55, 410.
- [42] J. van Wonderghem, S. Morup, S. W. Charles, S. Wells, *J. Colloid Interface Sci.* **1988**, 121, 558.
- [43] J. Park, K. An, Y. Hwang, J.-G. Park, H.-J. Noh, J.-Y. Kim, J.-H. Park, N.-M. Hwang, T. Hyeon, *Nat. Mater.* **2004**, 3, 891.
- [44] S. Peng, S. Sun, *Angew. Chem., Int. Ed.* **2007**, 46, 4155.
- [45] P. Podsiadlo, S. G. Kwon, B. Koo, B. Lee, V. B. Prakapenka, P. Dera, K. K. Zhuravlev, G. Krylova, E. V. Shevchenko, *J. Am. Chem. Soc.* **2013**, 135, 2435.
- [46] E. V. Shun'ko, V. S. Belkin, *J. Appl. Phys.* **2007**, 102, 083304.
- [47] Y. B. Lin, T. F. Chen, J. Tao, Y. Z. Shen, H. G. Li, *Surf. Eng.* **2015**, 31, 329.
- [48] Z. Wei Seh, W. Li, J. J. Cha, G. Zheng, Y. Yang, M. T. McDowell, P.-C. Hsu, Y. Cui, *Nat. Commun.* **2013**, 4, 1331.
- [49] J. Li, H. Zeng, S. Sun, J. P. Liu, Z. L. Wang, *J. Phys. Chem. B* **2004**, 108, 14005.
- [50] E. N. Maslen, V. A. Streltsov, N. R. Streltsova, *Acta Crystallogr., Sect. B: Struct. Crystallogr. Cryst. Chem.* **1994**, B50, 435.
- [51] K. Haneda, A. Morrish, *J. Phys., Colloq.* **1977**, 38, C1-321.
- [52] C. J. D. Hetherington, C. B. Boothroyd, R. E. Dunin-Borkowski, J. L. Hutchison, in *Proc. of the Institute of Physics Electron Microscopy and Analysis Group Conf.*, (Eds: M. Aindow, C. J. Kiely), Institute of Physics Publishing, Vol. 168, Dundee **2001**, pp. 55–58.
- [53] S. Mourdikoudis, L. M. Liz-Marzán, *Chem. Mater.* **2013**, 25, 1465.
- [54] R. A. Harris, P. M. Shumbula, H. Van Der Walt, *Langmuir* **2015**, 31, 3934.